Journal of Materials Science and Chemical Engineering, 2025, 13(9), 12-30
https://www.scirp.org/journal/msce
ISSN Online: 2327-6053
ISSN Print: 2327-6045

Fabrication and Characterization of N-Doped TiO_2 Photoanode-Based Dye-Sensitized Solar Cells

Fikria Jabli, Raha Alshammari*

Department of Physics, College of Sciences, Qassim University, Buryadh, Saudi Arabia
Email: *ra.alshammari@qu.edu.sa

How to cite this paper: Jabli, F. and Alshammari, R. (2025) Fabrication and Characterization of N-Doped TiO_2 Photoanode-Based Dye-Sensitized Solar Cells. *Journal of Materials Science and Chemical Engineering*, **13**, 12-30.
https://doi.org/10.4236/msce.2025.139002

Received: July 25, 2025
Accepted: September 2, 2025
Published: September 5, 2025

Abstract

Numerous studies have investigated the incorporation of transition metals such as Ag, Co, Mn, Zn, Cr, Nb, W, and Cu into TiO_2 to evaluate their optoelectronic properties. Previous research indicates that the introduction of transition metal ions into the TiO_2 lattice can effectively modulate various electronic characteristics, including band gap energy, Fermi level, d-electron configuration, and band positions. Moreover, studies have indicated that doping TiO_2 with non-metals like N, C, B, S, and F can reduce the band gap and enhance light absorption in the visible spectrum. Besides individual research on the metallic and non-metallic doping of TiO_2, studies have focused on their combined co-doping in TiO_2 for solar cell applications. For example, DSSCs incorporating Cu/N and Cu/S co-doped TiO_2 demonstrated notable performance improvements. In this work, we present our investigation into the structural, morphological, and optical properties of N-doped TiO_2 nanomaterials. The properties of the synthesized nanoparticles were assessed using X-ray diffraction (XRD), scanning electron microscopy (SEM), and UV-Visible spectroscopy. XRD data confirmed that both undoped and N-doped TiO_2 samples exhibit analogous peaks for anatase and rutile phases, indicating that nitrogen doping did not induce any TiO_2 phase transitions. SEM images of the pure and N-doped TiO_2 fabricated films depict a well-dispersed microstructure and a consistent grain distribution. Moreover, the band gap (E_g) and Urbach (E_u) energies were observed to be lower for the synthesized nanoparticles. The data indicated a decrease in E_g energy with nitrogen doping.

Keywords

Fabrication, Characterization, N-Doped TiO_2, Photoanode, Dye Sensitized, Solar Cells

1. Introduction

Dye-sensitized solar cells (DSSCs) represent a promising alternative to traditional silicon-based solar cells due to their cost-effectiveness, simple manufacturing process, ability to function in low-light conditions, and eco-friendly characteristics [1]. In DSSCs, Titanium dioxide (TiO_2) is widely used as the semiconductor material and photocatalyst due to its excellent electronic and optical properties [2]-[6]. However, the wide band gap of TiO_2 (3.2 eV) and its limited electron-hole pair transport capabilities hinder its practical application in DSSCs [7] [8]. To address these limitations, doping is recognized as a crucial strategy to improve the electrical and optical properties of TiO_2-based DSSCs by enhancing visible-light absorption, reducing the band gap, and enhancing charge carrier mobility [9].

Previous studies have explored the potential improvements in photovoltaic efficiency by utilizing nitrogen (N) doped TiO_2 nanoparticles, as they have a notable impact on DSSC performance [10] [11]. These works have shown that the incorporation of nitrogen as a dopant into TiO_2 can enhance electron transport characteristics and broaden light absorption across the visible range of the solar spectrum.

In this regard, we initially prepared N-doped TiO_2 nanoparticles through a solid-state reaction by varying the volumetric ratio between P25-TiO_2 and ammonium hydroxide (NH_4OH). Films were subsequently prepared from the resulting nanoparticles and sintered at 500˚C. Subsequently, the prepared N-doped TiO_2 nanoparticles were characterized structurally and optically, followed by an investigation of their charge transport characteristics and the PV performance of DSSCs based on N-doped TiO_2 photoanode.

2. Materials and Methods

The fluorine-doped tin oxide (FTO) coated conducting glass sheets (sheet resistance 7.5 Ω/cm^2 and size 2×1 cm^2) were cleaned initially with soapy water and subsequently with distilled water and ethanol using an ultrasonic bath. The undoped and N-doped (with systematically varied N contents) TiO_2 films were prepared by grinding 100 mg of P_{25}-TiO_2 separately with 0, 10, 20, 30, and 40 μL of NH_4OH as nitrogen source, deionized (DI) water, 20 μL of acetylacetone, and a drop of Triton ™ X-100 into pastes followed by separately coating the resultant pastes via doctor blade method on the cleaned FTO glass sheets. The prepared undoped and N-doped TiO_2 films were dried and calcined at 500˚C for 30 minutes. The resultant films were separately soaked in 0.3 mM N719 dye solution, prepared by dissolving N719 dye in a mixture of acetonitrile and tert-butyl alcohol (50% v/v), for 12 hours. After the dye-sensitization process, the photoanodes were washed with acetonitrile to remove the unanchored dye molecules and dried. Then, the corresponding devices were assembled by employing N719 dye-coated undoped or N-doped TiO_2 photoanode, I^-/I^-_3 redox couple, and Pt-coated FTO glass sheet as dye-sensitized photoanode, electrolyte, and counter electrode, respectively. The electrolyte was prepared by dissolving 2.07 g of potassium iodide and 0.19 g of iodine into 25 mL of ethylene glycol, followed by stirring for 15 minutes until a homogeneous solution rich in iodide/triiodide ions (I^-/I_3^-) was obtained. This redox couple plays a crucial role in the charge transfer and regeneration of the dye. The active area of each device was defined as 0.25 cm^2 using a mechanical mask. The thickness of the TiO_2 photoanode films was measured by scanning electron microscopy (SEM) and found to be approximately 6.5 µm. Hereafter, the undoped TiO_2 is referred to as "pure TiO_2," and the N-doped TiO_2 with systematically varied N contents is referred to as 10N-TiO_2, 20N-TiO_2, 30N-TiO_2, and 40N-TiO_2, indicating the respective NH_4OH volumes used.

3. Results and Discussion

3.1. XRD Analysis

The structural analysis of both pure and nitrogen-doped TiO_2 films was examined using X-ray diffraction (XRD), and the corresponding XRD patterns are presented in **Figure 1**. These patterns reveal distinct peaks consistent with the crystalline structure of anatase TiO_2 (Anatase XRD JCPDS Card No. 21-1272) and rutile TiO_2 (Rutile JCPDS Card No. 21-1276) [12] [13]. Peaks related to the anatase phase were identified within the tetragonal $I4_1/amd$ space group (No. 141), while those associated with the rutile phase were indexed in the tetragonal $P4_2/mnm$ space group (No. 136). Phase identifications were carried out using 'X'Pert HighScore Plus' software. Notably, the XRD data presented in **Figure 1** confirmed that both undoped and N-doped TiO_2 samples exhibit analogous peaks for anatase and rutile phases, indicating no phase transition induced by nitrogen doping.

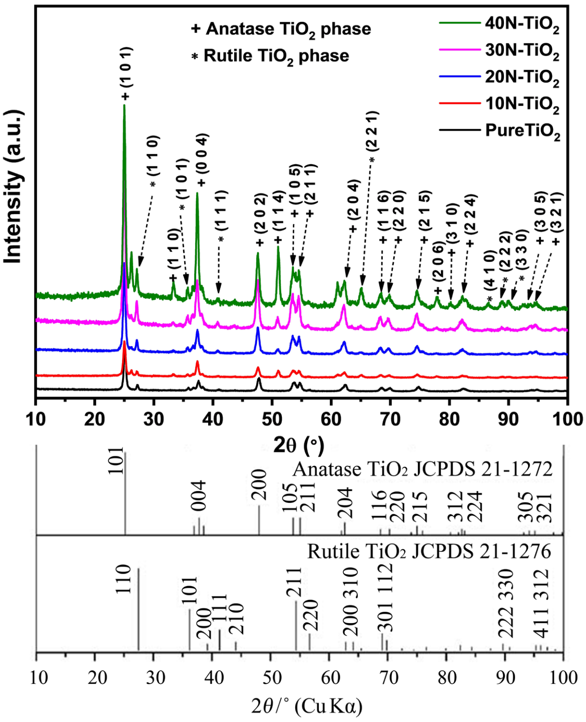

Figure 1. XRD patterns of pure and 10%, 20%, 30%, and 40% nitrogen-doped TiO_2 compared to those of the anatase and rutile TiO_2 phases.

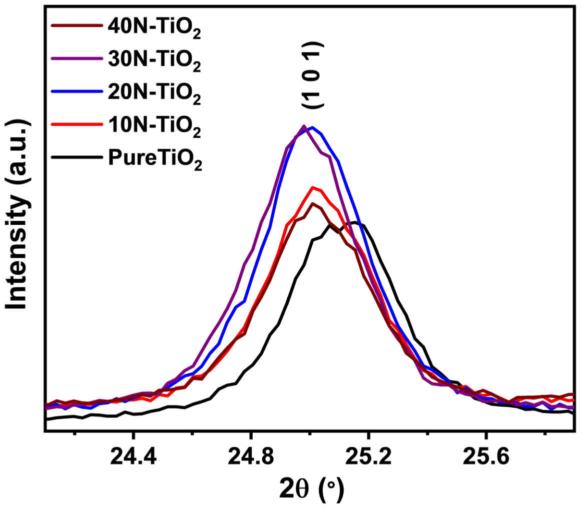

Figure 2. XRD profiles of the most intense peaks (1 0 1) of pure and 10%, 20%, 30%, and 40% N-doped TiO_2.

An enlargement of the most intense peak (1 0 1), as indicated in Figure 2, reveals a slight shift in the peak positions for the N-doped films towards lower diffraction angles (2θ) when compared to the pure TiO_2 sample. This change indicates successful incorporation of that nitrogen into the TiO_2 structure. Nitrogen was incorporated into titanium dioxide using the mixing method. Varying proportions of nitrogen were added to the chemical mixture using a graduated dropper. The successful incorporation of nitrogen into the material was confirmed by X-ray Diffraction (XRD) analysis. The resulting pattern showed a shift in the angles and peaks, which is indicative of nitrogen successfully integrating into the crystal lattice of the titanium dioxide [14]. The crystallite sizes (D) of the prepared thin films were calculated using the following Scherrer equation [15]:

$$D = \frac{K\lambda}{\beta\cos(\theta)} \tag{1}$$

Here, $\lambda = 1.5406$ Å denotes the X-ray wavelength, θ represents the Bragg angle associated with the anatase (101) peak, β indicates the line broadening at half the maximum intensity (FWHM), and $K = 0.9$ is referred to as the Scherrer constant. Table 1 shows the different parameters used in the Scherrer formula as well as the evolution of the crystallite size of the different samples. The estimated crystallite sizes (D) of all samples are found to be approximately 25 nm, indicating a nanoscale morphology of the synthesized materials. The findings presented in Table 1 demonstrate that there were minimal variations in the crystallite size across varying levels of N-doping content. This suggests that the introduction of nitrogen into the TiO_2 structure did not significantly alter the crystallite size of the material. This is consistent with previous studies [16] [17]. The lack of significant variation in crystallite size with different N-doping levels in TiO_2 suggests that nitrogen incorporation primarily modifies electronic properties, such as light absorption, without disrupting crystallite formation.

Table 1. Values of the different parameters allowing the calculation of crystallite size using the Scherrer formula.

Sample	2θ (°)	$\beta \times 10^{-2}$ (rd)	D (nm)
Pure TiO_2	25.122	5.709	24.88
10N-TiO_2	25.019	5.724	24.81
20N-TiO_2	25.006	5.721	24.83
30N-TiO_2	24.979	5.726	24.80
40N-TiO_2	25.011	5.722	24.82

3.2. Morphological Analysis

Figures 3(a)-(e) show SEM images of the pure and N-doped TiO_2 fabricated films, illustrating a well-dispersed microstructure and a consistent distribution of grains. The images exhibit both uniform and clustered grains, suggesting strong cohesion among individual particles and enhancing structural integrity [18]. Some minor voids are noticeable, which is expected due to the material's porous nature. A high calcination temperature of 500˚C was employed during sample synthesis to improve crystallinity and achieve a more uniform microstructure. This elevated temperature facilitated grain enlargement, leading to enhanced crystalline properties. Furthermore, the SEM images of the pure and N-doped TiO_2 films reveal that these nanoparticles exhibit spherical morphology.

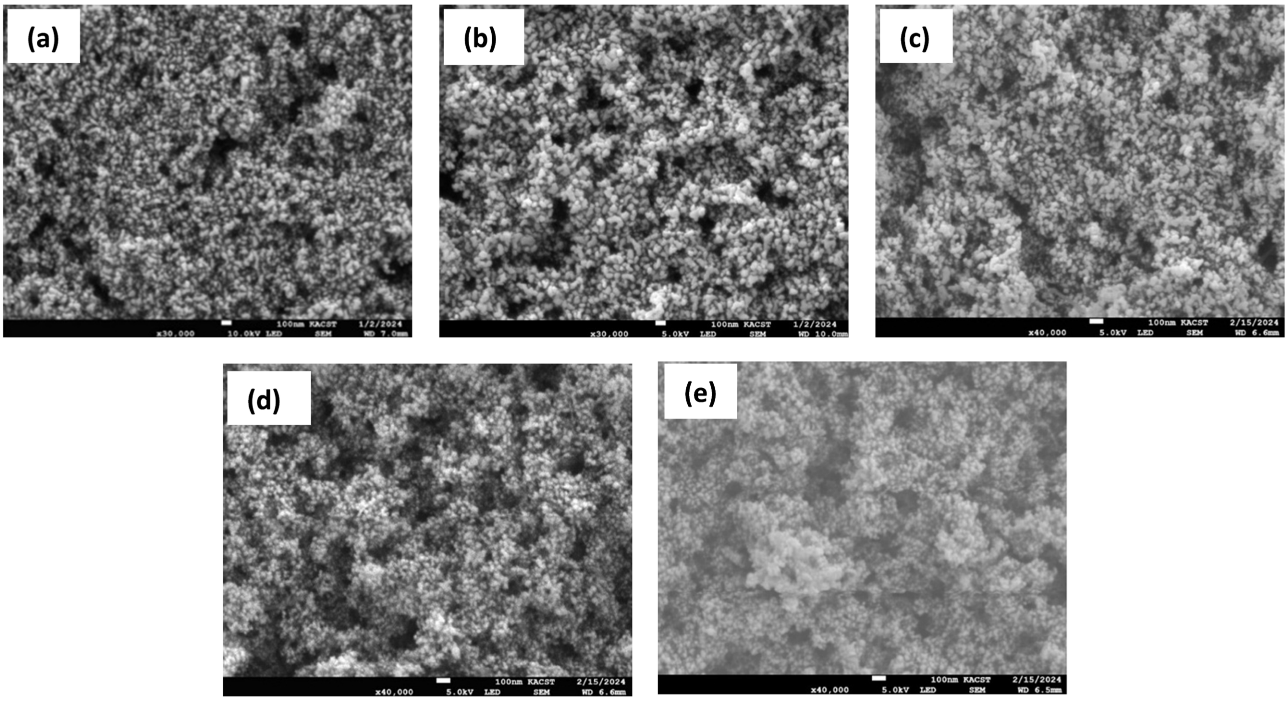

Figure 3. SEM images describing the surface morphology of pure and N-doped TiO_2 films: (a) Pristine TiO_2, (b) 10% N-doped TiO_2, (c) 20% N-doped TiO_2, (d) 30% N-doped TiO_2, and (e) 40% N-doped TiO_2.

By employing the Image J software to analyze the SEM images (refer to **Figure 4**), we calculated the average grain size for each sample. Consistent with the XRD analysis, there is no significant variation in the average grain size. This result is consistent with previously reported findings for similar materials [19]. The estimated sizes of the grains for both undoped and N-doped TiO_2 nanoparticles fall within the range of 40 nm to 45 nm. In contrast, the XRD patterns reveal smaller average crystallite sizes compared to those observed in the SEM images due to agglomeration caused by higher surface area-to-volume ratios [20]. This process merges crystallites into larger grains. Higher calcination temperatures enhance grain growth and the aggregation of adjacent grains into larger particles, reducing the system's Gibbs free energy by minimizing the extended surface area [21].

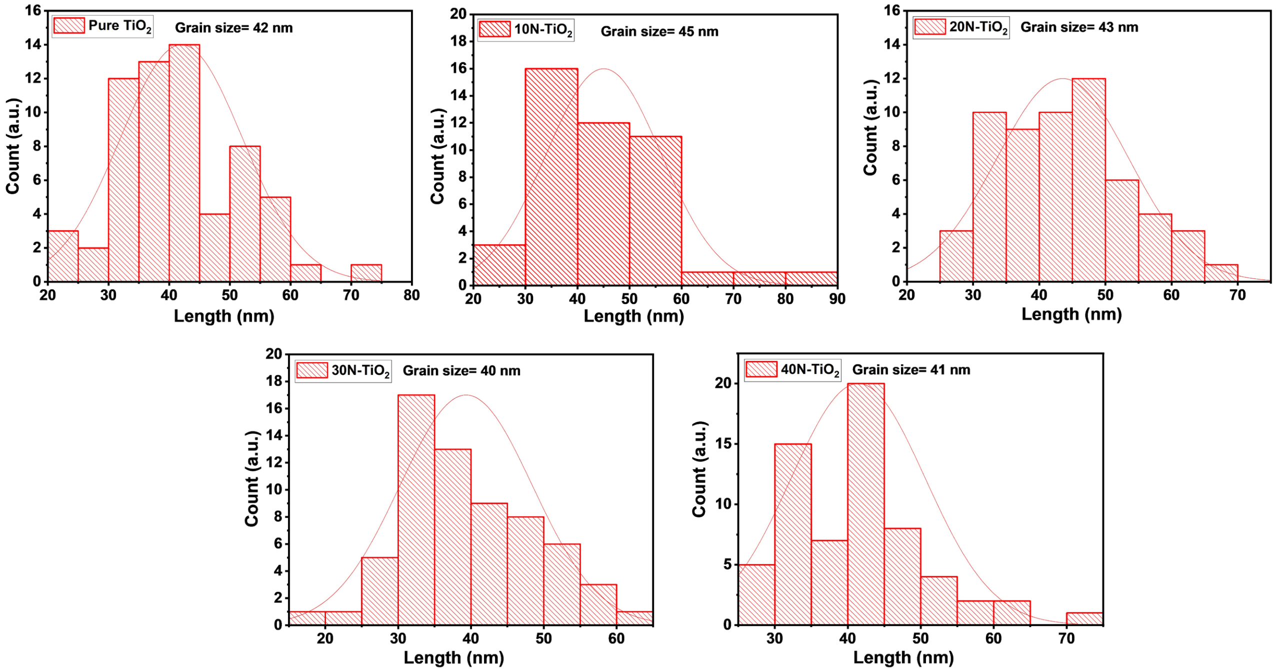

Figure 4. Histograms of grain size distribution: (a) Pristine TiO_2, (b) 10% N-doped TiO_2, (c) 20% N-doped TiO_2, (d) 30% N-doped TiO_2, and (e) 40% N-doped TiO_2.

3.3. Optical Properties

3.3.1. UV-VIS Absorbance Spectra

Figure 5 illustrates the absorbance (A) spectra versus wavelength (λ) for the pure and N-doped TiO_2 fabricated films within the UV (ultraviolet) and VIS (visible) radiation ranges. As depicted in this figure, the N-doped TiO_2 nanoparticles exhibit a progressive red shift towards higher wavelengths (red shift) in the UV-VIS regions as the N dopant concentration increases compared to pure TiO_2. This finding aligns with previous studies [22] [23]. Conversely, the spectra reveal two primary absorption bands in the UV-VIS regions. The presence of these spectral features indicates that the films are well-suited for absorbing both UV and visible light, making them versatile for various applications requiring such light absorption. These include UV-VIS light absorption, photocatalysis, and dye-sensitized solar cells (DSSCs) [24] [25]. In the realm of DSSCs, these prepared films have the potential to capture energy from absorbed UV and visible light, transforming it into electricity. Their ability to capture a wide range of wavelengths enhances their effectiveness in converting light energy into electrical power. Furthermore, in the context of photocatalysis, these samples can act as catalysts to accelerate chemical reactions when exposed to either UV or visible light.

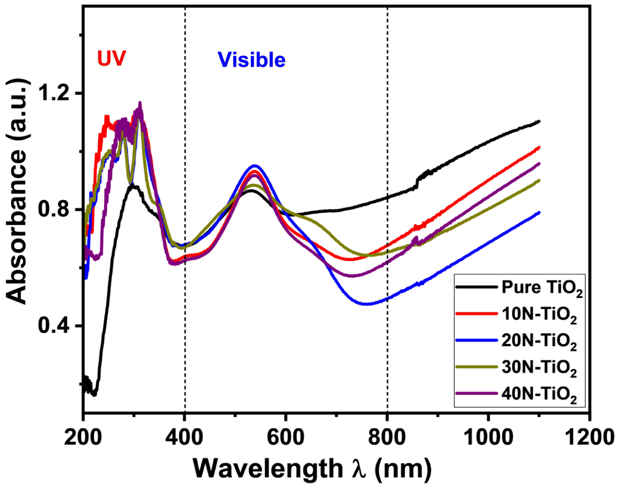

Figure 5. UV-Vis spectra for the pure TiO_2, 10% N-doped TiO_2, 20% N-doped TiO_2, 30% N-doped TiO_2, and 40% N-doped TiO_2.

The optical absorption coefficient (α) of the fabricated films was calculated through Equation (2), and the Tauc law, as defined in Equation (3) [26], was employed to determine the band gap energy (E_g) values for both the pure TiO_2 and N-doped TiO_2 films. Additionally, Equation (4) is employed to verify the optical transitions occurring within the samples.

$$\alpha = \frac{2.303 \times A}{d} \tag{2}$$

$$\left(\alpha h\nu\right)^{1/n} = \beta\left(h\nu - E_g\right) \tag{3}$$

$$\ln\left(\alpha h\nu\right) = \ln\left(\beta\right) + n\ln\left(h\nu - E_{gd}\right) \tag{4}$$

where $h\nu$ is the photon energy, d is the thickness of each sample, and A is the absorbance. From the [$(\alpha h\nu)^2$ vs. $h\nu$] curves shown in Figure 6, the direct (E_{gd}) band gap values were found to be 3.12, 3.04, 3.00, 2.96, and 2.93 eV for pure TiO_2, 10% N-doped TiO_2, 20% N-doped TiO_2, 30% N-doped TiO_2, and 40% N-doped TiO_2, respectively.

The plot of [ln($\alpha h\nu$) vs. ln($h\nu - E_g$)] in Figure 7 reveals that the n exponent values are close to 0.5 for the prepared films. This suggests that both the undoped and N-doped TiO_2 nanoparticles exhibit direct optical transitions. This indicates a direct band gap, allowing electrons to transition from the valence band to the conduction band without intermediate energy levels. This distinctive feature, together with their exceptional light absorption and emission qualities, renders these materials promising candidates for use in dye-sensitized solar cells and optoelectronic devices.

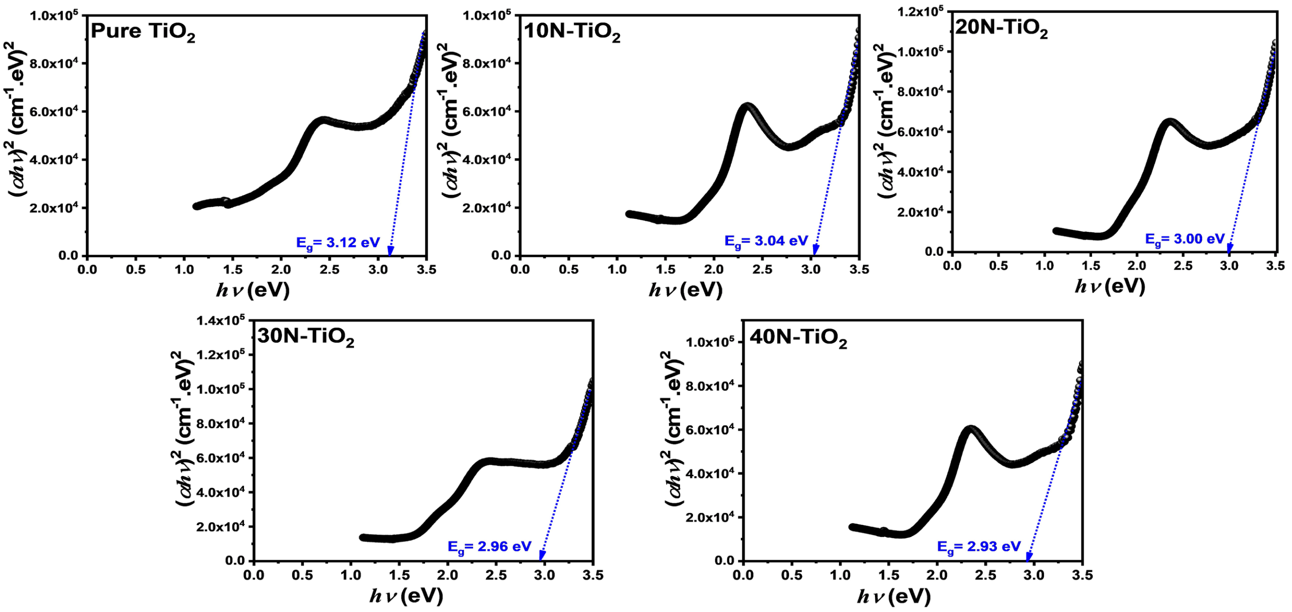

Figure 6. Plots of $(\alpha h\nu)^2$ versus $h\nu$ for the pure TiO$_2$, 10% N-doped TiO$_2$, 20% N-doped TiO$_2$, 30% N-doped TiO$_2$, and 40% N-doped TiO$_2$.

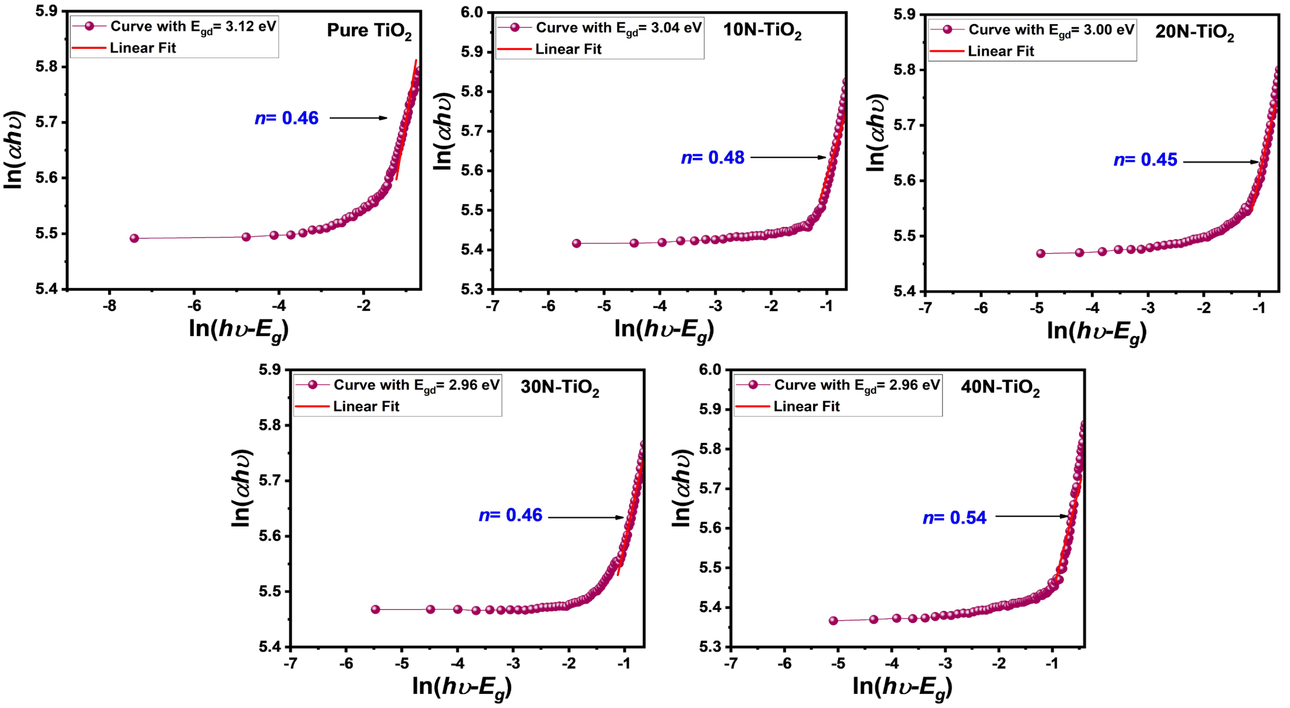

Figure 7. Plots of $\ln(\alpha h\nu)$ versus $\ln(h\nu - E_g)$ for the pure TiO$_2$, 10% N-doped TiO$_2$, 20% N-doped TiO$_2$, 30% N-doped TiO$_2$, and 40% N-doped TiO$_2$.

Table 2. Comparison of band gap energies for the pure and N-doped TiO_2 films with literature values.

Sample	Band Gap Energy (eV)	Reference
TiO_2	3.20	[34]
ZnO	3.37	[35]
CuO	3.85	[36]
TiO_2	3.21	[37]
25N-TiO_2	3.07	[37]
TiO_2	3.15	[38]
20N-TiO_2	3.03	[38]
TiO_2	3.56	[39]
5Ni-TiO_2	3.39	[39]
10Ni-TiO_2	3.34	[39]
TiO_2	3.41	[40]
2Cu-TiO_2	3.42	[40]
6Cu-TiO_2	3.22	[40]
10Cu-TiO_2	3.31	[40]
TiO_2	3.12	This work
10N-TiO_2	3.04	This work
20N-TiO_2	3.00	This work
30N-TiO_2	2.96	This work
40N-TiO_2	2.93	This work

The energy band gap values (E_g) of both undoped and N-doped TiO_2 films are compared in **Table 2** with those of various semiconductors [27]-[29] and other TiO_2 films with different dopants [30]-[32]. The data indicated that the E_g energy decreases with nitrogen doping, aligning well with findings from other studies [17] [30]. This decrease in band gap energy resulting from nitrogen doping may stem from the formation of isolated narrow bands above TiO_2's valence band. This can occur by combining the 2p states of nitrogen and oxygen in the dopant and TiO_2 (interstitial doping), or by replacing oxygen-deficient sites with nitrogen (substitutional doping) [33] [34]. Consequently, the decrease in band gap energy may be attributed to the impurity levels generated above the valence band of TiO_2 through interstitial nitrogen doping. It has also been noted that interstitial nitrogen doping significantly impacts and diminishes the band gap of TiO_2 in comparison to substitutional N doping [35]. In addition, the E_g values of the fabricated films, as depicted in **Table 2**, are lower than those of other doped TiO_2 films, such as Ni-doped TiO_2 and Cu-doped TiO_2 [32]. Furthermore, the synthesized thin films have lower E_g values compared to wide-band gap semiconductors like ZnO, TiO_2, and CuO that absorb UV light [27]-[29]. Recent studies have focused on enhancing visible light absorption by developing materials with narrow band gap energies [36]. This makes the produced samples well-suited for capturing crucial visible light, which is essential for applications like solar cells and photocatalysis.

The observed decreases in both the direct (E_g) and indirect (E_u) band gaps are directly linked to the specific electronic states introduced by either interstitial or substitutional nitrogen. Interstitial nitrogen atoms introduce new energy levels deep within the band gap, providing additional pathways for electronic transitions and thus reducing both E_g and E_u. In contrast, substitutional nitrogen atoms replace host atoms, which modifies the overall electronic band structure and can lead to a general narrowing of the band gap. A recent study by Wang *et al.* (2024, Journal of Materials Science) supports this distinction, demonstrating that deep-level defects, primarily responsible for the significant reduction in band gap values, are predominantly formed by interstitial nitrogen, while substitutional nitrogen contributes more to the overall modification of the material's band structure [37].

3.3.2. Urbach Energy

Urbach energy (E_u) serves as a crucial parameter in optical spectroscopy for evaluating the degree of disorder and impurity levels in a material [38]. It provides insights into the localized states within the band gap and the broadening of electronic transitions, thereby reflecting the material's internal characteristics and electronic behavior. This energy value is associated with the exponential tail in the density of states near the band gap's edges. A lower E_u value indicates a material with higher orderliness and fewer defects, whereas a higher E_u value indicates a heightened presence of disorder and defect concentration. The determination of E_u energy from the photon energy ($h\nu$) can be carried out from the following equation [39]:

$$\alpha = \alpha_0 \exp\left(\frac{h\nu}{E_u}\right) \tag{5}$$

where α is the absorption coefficient and α_0 is a constant. By logarithmically transforming both sides of Equation (6), we can derive this relation:

$$\ln \alpha = \ln \alpha_0 + \frac{h\nu}{E_u} \tag{6}$$

This logarithmic representation is utilized for analyzing experimental data and extracting the E_u energy from the absorption spectra based on the [ln(α) vs. ($h\nu$)] curve. The Urbach energy is derived from the ln(α) vs. $h\nu$ curve by examining the linear segment located at the lower energy side of the absorption spectrum, below the band gap energy values. The determined E_u values for pure TiO_2, 10% N-doped TiO_2, 20% N-doped TiO_2, 30% N-doped TiO_2, and 40% N-doped TiO_2 nanoparticles were 1.75, 0.91, 1.04, 1.54, and 0.86 eV, respectively. The observed decrease in Urbach energy values upon nitrogen doping suggests a potential decrease in structural disorder and impurities within the TiO_2 sample. Additionally, lower Urbach energy values indicate a more organized material structure with fewer localized states within the band gap in the prepared samples. The variation of E_u with nitrogen doping is shown in **Figure 8**.

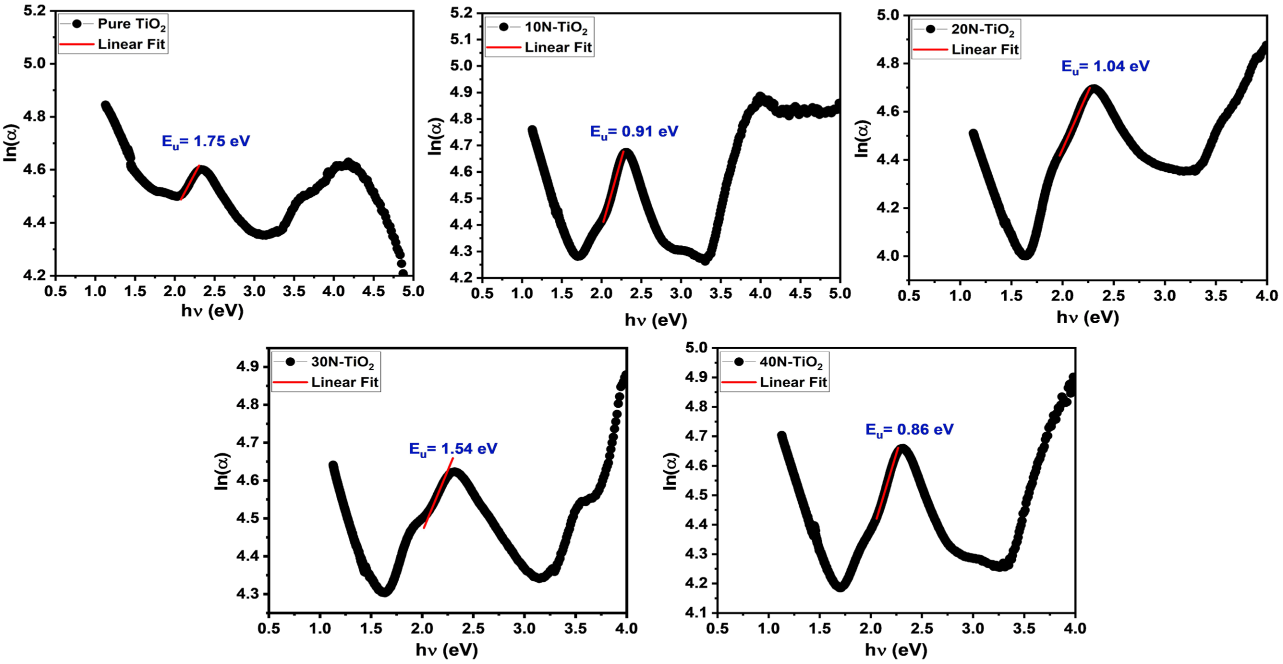

Figure 8. Plot of ln(α) versus ($h\nu$) for the pure TiO_2, 10% N-doped TiO_2, 20% N-doped TiO_2, 30% N-doped TiO_2, and 40% N-doped TiO_2.

3.3.3. Steepness Parameter and Electron-Phonon Interaction Energy

The Urbach energy (E_u) and the temperature-dependent steepness parameter $S(T)$ can be expressed through the following [40]:

$$E_u = \frac{k_B T}{S(T)} \tag{7}$$

In this equation, the symbol k_B denotes the Boltzmann constant, and T represents the standard room temperature. The steepness parameter, denoted as $S(T)$, quantifies the broadening of the absorption edge, which is attributed to various interactions such as electron-phonon or exciton-phonon couplings [41]. It measures how rapidly the absorption coefficient changes with photon energy in the vicinity of the band edge. A higher $S(T)$ value corresponds to a sharper absorption edge, indicating a wider energy range over which the absorption coefficient varies significantly. The calculated S values for the pure TiO_2, 10% N-doped TiO_2, 20% N-doped TiO_2, 30% N-doped TiO_2, and 40% N-doped TiO_2 nanoparticles were 0.014, 0.028, 0.024, 0.017, and 0.030, respectively. Significantly, the increased S value observed in the 10% N-doped TiO_2 sample indicates a greater broadening of the absorption edge compared to the remaining samples. Following Equation (8), the electron-phonon interaction energy (E_{e-ph}) can be estimated based on the S parameter, as follows [41]:

$$E_{e-ph}=\frac{2}{3S} \tag{8}$$

The E_{e-ph} value denotes the energy associated with the interaction between electrons and phonons in the material, serving as a significant parameter for understanding the material's electronic and thermal characteristics. A higher E_{e-ph}-value indicates a stronger electron-phonon interaction, indicating a greater propensity for energy dissipation through lattice vibrations. In our study, utilizing Equation (8), we have computed the E_{e-ph} values for our samples as 47.62, 23.81, 27.78, 39.22, and 22.22 eV for the pure TiO_2, 10% N-doped TiO_2, 20% N-doped TiO_2, 30% N-doped TiO_2, and 40% N-doped TiO_2 films, respectively. The heightened E_{e-ph} value observed in the pure TiO_2 sample indicates a stronger electron-phonon interaction and a higher likelihood for energy dissipation through lattice vibrations compared to the N-doped TiO_2 films.

3.3.4. Threshold Wavelength

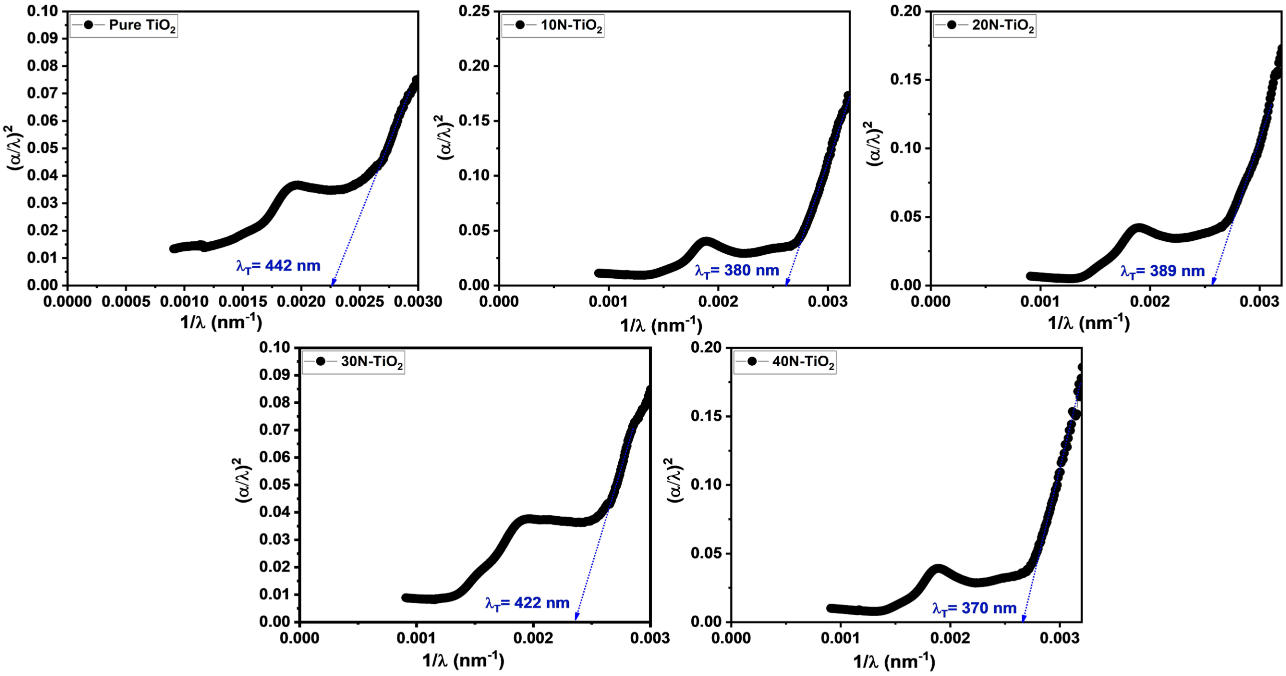

Figure 9. Plots of $(\alpha/\lambda)^2$ versus $1/\lambda$ for the pure TiO_2, 10% N-doped TiO_2, 20% N-doped TiO_2, 30% N-doped TiO_2, and 40% N-doped TiO_2.

In optoelectronic devices, the critical wavelength (λ_T), also known as the threshold wavelength, plays a significant role in evaluating a material's suitability for such applications by representing the maximum wavelength of incident radiation. This λ_T parameter signifies the shortest wavelength of light essential to trigger particular optoelectronic operations, like absorption or emission, within a material. To calculate the λ_T value, we have applied the following equation [42]:

$$\left(\frac{\alpha}{\lambda}\right)^2=C\left(\frac{1}{\lambda}\right)-\left(\frac{1}{\lambda_T}\right) \tag{9}$$

where α represents the absorption coefficient, λ stands for the wavelength of incoming radiation, and C is a constant, the threshold wavelength (λ_T) values were determined as 442, 380, 389, 422, and 370 nm for the pure TiO_2, 10% N-doped TiO_2, 20% N-doped TiO_2, 30% N-doped TiO_2, and 40% N-doped TiO_2 films, respectively, as indicated in **Figure 9**. The variation of λ_T values closely aligns with the band gap energy values. Typically, a lower band gap energy corresponds to a reduced λ_T value. This suggests that the 40% N-doped TiO_2 sample necessitates higher-energy photons (shorter wavelengths) to initiate optoelectronic processes.

3.3.5. Penetration Depth

The penetration depth (δ) acts as a measure that defines the distance to which incoming light or radiation can permeate within a substance. According to Equation (10) [43], the δ parameter can be estimated as follows:

$$\delta = \frac{1}{\alpha(\lambda)} \tag{10}$$

The data illustrated in **Figure 10** reveal that the determined penetration depth values ($\delta(\lambda)$) are significantly reduced in the fabricated films. This indicates that the samples may be promising for photovoltaic purposes due to improved light absorption and potentially increased energy conversion efficiency resulting from the decreased penetration depth. Furthermore, their decreased penetration depth makes them ideal candidates for advanced photodetectors, enabling the precise detection of light spanning a wide range of wavelengths.

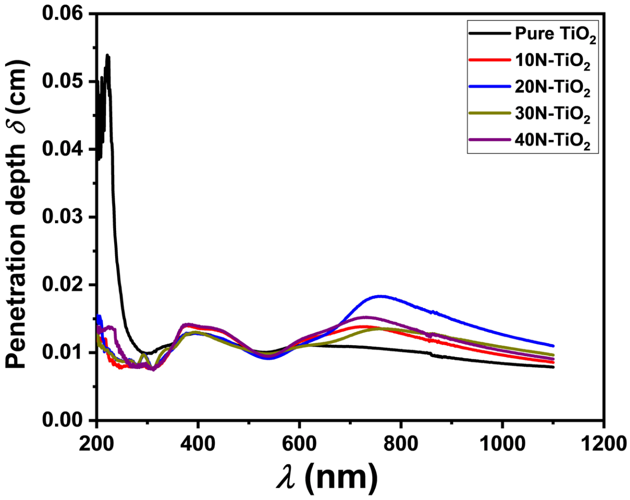

Figure 10. Penetration depth (δ) versus λ for the pure TiO_2, 10% N-doped TiO_2, 20% N-doped TiO_2, 30% N-doped TiO_2, and 40% N-doped TiO_2.

3.3.6. Extinction Coefficient

The extinction coefficient (k) provides valuable insights into how light is absorbed and scattered within a material, indicating the material's effectiveness in diminishing the intensity of incident radiation. This coefficient reflects both the absorption and scattering processes that contribute to the overall attenuation of light.

According to Equation (11) [44], the extinction coefficient (k) can be calculated using the following formula:

$$k = \frac{\alpha\lambda}{4\pi} \tag{11}$$

Figure 11 displays the variation of the coefficient k versus photon energy ($h\nu$) across the different types of films: pure TiO_2, 10% N-doped TiO_2, 20% N-doped TiO_2, 30% N-doped TiO_2, and 40% N-doped TiO_2. It should be noted that k-values are higher at lower $h\nu$ values but decrease significantly as $h\nu$ rises, eventually approaching zero. This trend suggests minimal light loss in the higher energy range. Similar patterns of decreasing k values with rising photon energy have been noted in diverse materials [45] [46], implying that the prepared samples allow light to pass through with minimal loss. The variations in k values are around 10^{-5}, indicating that losses from scattering and absorption during light transmission through the samples are negligible. This behavior highlights the high transparency of the films. Importantly, these findings align with prior research by Mott and Davis [47].

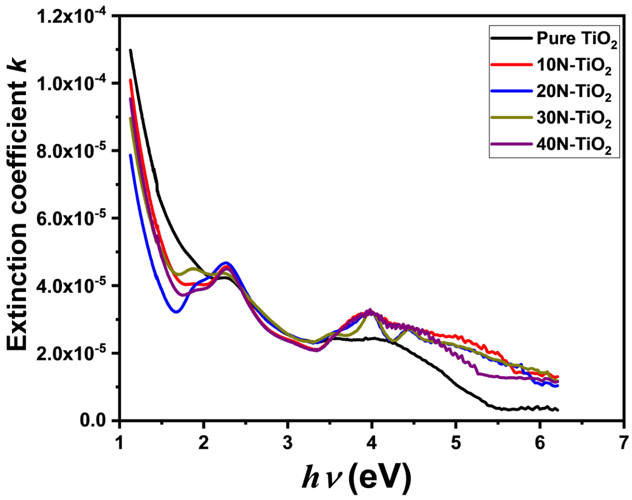

Figure 11. Extinction coefficient (k) versus $h\nu$ for the pure TiO_2, 10% N-doped TiO_2, 20% N-doped TiO_2, 30% N-doped TiO_2, and 40% N-doped TiO_2.

4. Conclusions

In this study, Nitrogen-doped TiO_2 nanoparticles were successfully synthesized and characterized. Analysis of XRD patterns confirmed that the TiO_2 anatase and rutile crystal structures remained unchanged after N doping. SEM images demonstrated nanoparticle agglomeration influenced by the N dopant concentration. Furthermore, both the band gap (E_g) and Urbach (E_u) energies were observed to be decreased for the synthesized nanoparticles. The data clearly show a decrease in E_g energy with nitrogen doping. The decreasing trend in Urbach energy values with N-doping suggests a potential reduction in disorder, defects, or impurities within the TiO_2 sample. A comprehensive study of optical parameters, including penetration depth, threshold wavelength, and extinction coefficients, was also conducted. The findings indicated that nitrogen doping in Titanium dioxide (TiO_2) improves its visible light absorption. These doped nanoparticles offer several benefits, including cost-effective production, lower band gap energies, high transparency, effective light absorption, and efficient energy conversion. Overall, the nitrogen-doped TiO_2 exhibits strong potential for various optoelectronic applications, particularly in technologies such as DSSCs and photocatalysis, where absorbing visible light is crucial for energy conversion and catalyzing reactions.

Limitations and Suggestions

While high concentrations of nitrogen doping are known to enhance the electrochemical properties of titanium dioxide-coated anodes, particularly their performance in lithium-ion batteries, excessive nitrogen levels can lead to several undesirable consequences. Over-doping with nitrogen can induce lattice distortions in the titanium dioxide crystal structure, which may reduce its long-term stability. High nitrogen concentrations can also create unwanted defects or new, unstable phases, hinder lithium-ion diffusion, and negatively impact the battery's charge and discharge rates. Furthermore, high nitrogen levels might decrease the material's effective surface area, limiting available reaction sites for lithium ions and ultimately affecting the overall battery capacity. Future Experiment to Address These Drawbacks. To mitigate these challenges, we propose a future experiment focused on co-doping techniques. This study would evaluate the combined effect of doping with nitrogen and a second element, such as carbon or fluorine, to stabilize the titanium dioxide lattice. The experiment would involve preparing several anode groups:

- A control group with an undoped anode.
- Groups were doped with nitrogen only at varying concentrations (low, medium, and high).
- Groups co-doped with nitrogen and the second element at different ratios.

We would then perform comprehensive analyses, including X-ray diffraction (XRD) to study crystal structure stability, X-ray photoelectron spectroscopy (XPS) to examine surface chemical composition, and galvanostatic cycling to measure key electrochemical properties like capacity and cycle life. We anticipate that co-doping will improve the anode's performance more effectively than nitrogen doping alone, helping to identify the optimal nitrogen concentration that enhances performance without compromising structural integrity [48].

Conflicts of Interest

The authors declare no conflicts of interest regarding the publication of this paper.

References

[1] Rajaramanan, T., Shanmugaratnam, S., Gurunanthanan, V., Yohi, S., Velauthapillai, D., Ravirajan, P., *et al.* (2021) Cost Effective Solvothermal Method to Synthesize Zn-Doped TiO_2 Nanomaterials for Photovoltaic and Photocatalytic Degradation Applications. *Catalysts*, **11**, Article 690. https://doi.org/10.3390/catal11060690

[2] Huang, F., Yan, A. and Zhao, H. (2016) Influences of Doping on Photocatalytic Properties of TiO_2 Photocatalyst. In: *Semiconductor Photocatalysis—Materials, Mechanisms and Applications*, InTech, 31.

[3] Park, S.K., Jeong, J.S., Yun, T.K. and Bae, J.Y. (2015) Preparation of Carbon-Doped TiO_2 and Its Application as a Photoelectrodes in Dye-Sensitized Solar Cells. *Journal of Nanoscience and Nanotechnology*, **15**, 1529-1532. https://doi.org/10.1166/jnn.2015.9338

[4] Rajaramanan, T., Natarajan, M., Ravirajan, P., Senthilnanthanan, M. and Velauthapillai, D. (2020) Ruthenium (Ru) Doped Titanium Dioxide (P25) Electrode for Dye Sensitized Solar Cells. *Energies*, **13**, Article 1532. https://doi.org/10.3390/en13071532

[5] Pirashanthan, A., Murugathas, T., Mariappan, K., Ravirajan, P., Velauthapillai, D. and Yohi, S. (2020) A Multifunctional Ruthenium Based Dye for Hybrid Nanocrystalline Titanium Dioxide/Poly(3-Hexylthiophene) Solar Cells. *Materials Letters*, **274**, Article 127997. https://doi.org/10.1016/j.matlet.2020.127997

[6] Siva, U., Murugathas, T., Yohi, S., Natarajan, M., Velauthapillai, D. and Ravirajan, P. (2020) Single Walled Carbon Nanotube Incorporated Titanium Dioxide and Poly(3-Hexylthiophene) as Electron and Hole Transport Materials for Perovskite Solar Cells. *Materials Letters*, **276**, Article 128174. https://doi.org/10.1016/j.matlet.2020.128174

[7] Kajana, T., Velauthapillai, D., Shivatharsiny, Y., Ravirajan, P., Yuvapragasam, A. and Senthilnanthanan, M. (2020) Structural and Photoelectrochemical Characterization of Heterostructured Carbon Sheet/Ag_2MoO_4-SnS/Pt Photocapacitor. *Journal of Photochemistry and Photobiology A*: *Chemistry*, **401**, Article 112784. https://doi.org/10.1016/j.jphotochem.2020.112784

[8] Dette, C., Pérez-Osorio, M.A., Kley, C.S., Punke, P., Patrick, C.E., Jacobson, P., *et al.* (2014) TiO_2 Anatase with a Band gap in the Visible Region. *Nano Letters*, **14**, 6533-6538. https://doi.org/10.1021/nl503131s

[9] Akila, Y., Muthukumarasamy, N. and Velauthapillai, D. (2019) TiO_2-Based Dye-Sensitized Solar Cells. In: *Nanomaterials for Solar Cell Applications*, Elsevier, 127-144. https://doi.org/10.1016/b978-0-12-813337-8.00005-9

[10] Guo, W., Shen, Y., Boschloo, G., Hagfeldt, A. and Ma, T. (2011) Influence of Nitrogen Dopants on N-Doped TiO_2 Electrodes and Their Applications in Dye-Sensitized Solar Cells. *Electrochimica Acta*, **56**, 4611-4617. https://doi.org/10.1016/j.electacta.2011.02.091

[11] Ma, T., Akiyama, M., Abe, E. and Imai, I. (2005) High-Efficiency Dye-Sensitized Solar Cell Based on a Nitrogen-Doped Nanostructured Titania Electrode. *Nano Letters*, **5**, 2543-2547. https://doi.org/10.1021/nl051885l

[12] Karthik, T., Rathinamoorthy, R. and Murugan, R. (2012) Enhancement of Wrinkle Recovery Angle of Cotton Fabric Using Citric Acid Cross-Linking Agent with Nano-TiO_2 as a Co-Catalyst. *Journal of Industrial Textiles*, **42**, 99-117. https://doi.org/10.1177/1528083711427481

[13] Masuda, Y. and Kato, K. (2009) Synthesis and Phase Transformation of TiO_2 Nano-Crystals in Aqueous Solutions. *Journal of the Ceramic Society of Japan*, **117**, 373-376. https://doi.org/10.2109/jcersj2.117.373

[14] Lee, J.K., Choi, W., Yoon, S. and Kim, J. (2011) Effects of Nitrogen Doping on the Crystal Structure and Electrochemical Properties of TiO_2 for Lithium-Ion Battery Anodes. *Electrochimica Acta*, **56**, 4591-4598.

[15] Mehnane, H.F., Wang, C., Kondamareddy, K.K., Yu, W., Sun, W., Liu, H., *et al.* (2017) Hydrothermal Synthesis of TiO_2 Nanoparticles Doped with Trace Amounts of Strontium, and Their Application as Working Electrodes for Dye Sensitized Solar Cells:

Tunable Electrical Properties & Enhanced Photo-Conversion Performance. *RSC Advances*, **7**, 2358-2364. https://doi.org/10.1039/c6ra26012h

[16] Sinhmar, A., Setia, H., Kumar, V., Sobti, A. and Toor, A.P. (2020) Enhanced Photocatalytic Activity of Nickel and Nitrogen Co-Doped TiO_2 under Sunlight. *Environmental Technology & Innovation*, **18**, Article 100658. https://doi.org/10.1016/j.eti.2020.100658

[17] Rajaramanan, T., Kumara, G.R.A., Velauthapillai, D., Ravirajan, P. and Senthilnanthanan, M. (2021) Ni/N Co-Doped P25 TiO_2 Photoelectrodes for Efficient Dye-Sensitized Solar Cells. *Materials Science in Semiconductor Processing*, **135**, Article 106062. https://doi.org/10.1016/j.mssp.2021.106062

[18] Saleem, S., Jameel, M.H., Alothman, A.A., Mayzan, M.Z.H.B., Yousaf, T., Ahmad, M.R., *et al.* (2024) A Band Gap Engineering for the Modification in Electrical Properties of Fe_3O_4 by Cu^{2+} Doping for Electronic and Optoelectronic Devices Applications. *Journal of Sol-Gel Science and Technology*, **109**, 471-482. https://doi.org/10.1007/s10971-023-06287-4

[19] Rajaramanan, T., Velauthapillai, D., Ravirajan, P. and Senthilnanthanan, M. (2023) A Facile Impregnation Synthesis of Ni-Doped TiO_2 Nanomaterials for Dye-Sensitized Solar Cells. *Journal of Materials Science: Materials in Electronics*, **34**, Article No. 916. https://doi.org/10.1007/s10854-023-10347-4

[20] Rhaman, M.M., Matin, M.A., Hakim, M.A. and Islam, M.F. (2021) Band gap Tuning of Samarium and Cobalt Co-Doped Bismuth Ferrite Nanoparticles. *Materials Science and Engineering: B*, **263**, Article 114842. https://doi.org/10.1016/j.mseb.2020.114842

[21] Basak, M., Rahman, M.L., Ahmed, M.F., Biswas, B. and Sharmin, N. (2021) Calcination Effect on Structural, Morphological and Magnetic Properties of Nano-Sized $CoFe_2O_4$ Developed by a Simple Co-Precipitation Technique. *Materials Chemistry and Physics*, **264**, Article 124442. https://doi.org/10.1016/j.matchemphys.2021.124442

[22] Kang, S.H., Kim, H.S., Kim, J. and Sung, Y. (2010) Enhanced Photocurrent of Nitrogen-Doped TiO_2 Film for Dye-Sensitized Solar Cells. *Materials Chemistry and Physics*, **124**, 422-426. https://doi.org/10.1016/j.matchemphys.2010.06.059

[23] Lin, Y.H., Weng, C.H., Srivastav, A.L., Lin, Y.T. and Tzeng, J.H. (2015) Facile Synthesis and Characterization of N-Doped TiO_2 Photocatalyst and Its Visible-Light Activity for Photo-Oxidation of Ethylene. *Journal of Nanomaterials*, **2015**, Article 807394. https://doi.org/10.1155/2015/807394

[24] Raddaoui, G., Rejaiba, O., Nasri, M., Khirouni, K., Alzahrani, B., Bouazizi, M.L., *et al.* (2022) Investigation Studies of Structural, Electrical, Dielectric, and Optical of $DyTi_{0.5}Mn_{0.5}O_3$ Multiferroic for Optoelectronics Applications. *Journal of Materials Science: Materials in Electronics*, **33**, 21890-21912. https://doi.org/10.1007/s10854-022-08976-2

[25] Wang, J., Zhang, C., Liu, H., McLaughlin, R., Zhai, Y., Vardeny, S.R., *et al.* (2019) Spin-Optoelectronic Devices Based on Hybrid Organic-Inorganic Trihalide Perovskites. *Nature Communications*, **10**, Article No. 129. https://doi.org/10.1038/s41467-018-07952-x

[26] Jameel, M.H., Mayzan, M.Z.H.B., Roslan, M.S.B., Zuhan, M.K.N.B.M., Rizvi, S.Z.H., Agam, M.A.B., *et al.* (2024) Experimental and Theoretical DFT Study of Hydrothermally Synthesized MoS_2-Doped-TiO_2 Nanocomposites for Photocatalytic Application. *Journal of Photochemistry and Photobiology A: Chemistry*, **448**, Article 115334. https://doi.org/10.1016/j.jphotochem.2023.115334

[27] Subudhi, S., Mahapatra, A., Mandal, M., Das, S., Sa, K., Alam, I., *et al.* (2020) Effect of Co Doping in Tuning the Band Gap of $LaFeO_3$. *Integrated Ferroelectrics*, **205**, 61-65. https://doi.org/10.1080/10584587.2019.1674998

[28] Xie, J., Wang, H., Duan, M. and Zhang, L. (2011) Synthesis and Photocatalysis Properties of ZnO Structures with Different Morphologies via Hydrothermal Method. *Applied Surface Science*, **257**, 6358-6363. https://doi.org/10.1016/j.apsusc.2011.01.105

[29] Jia, L., Li, J. and Fang, W. (2009) Enhanced Visible-Light Active C and Fe Co-Doped $LaCoO_3$ for Reduction of Carbon Dioxide. *Catalysis Communications*, **11**, 87-90. https://doi.org/10.1016/j.catcom.2009.08.016

[30] Jadhav, P.S., Jadhav, T., Bhosale, M., Jadhav, C.H. and Pawar, V.C. (2021) Structural and Optical Properties of N-Doped TiO_2 Nanomaterials. *Materials Today: Proceedings*, **43**, 2763-2767. https://doi.org/10.1016/j.matpr.2020.07.164

[31] Tian, J., Gao, H., Deng, H., Sun, L., Kong, H., Yang, P., *et al.* (2013) Structural, Magnetic and Optical Properties of Ni-Doped TiO_2 Thin Films Deposited on Silicon (100) Substrates by Sol-Gel Process. *Journal of Alloys and Compounds*, **581**, 318-323. https://doi.org/10.1016/j.jallcom.2013.07.105

[32] Bensouici, F., Bououdina, M., Dakhel, A.A., Tala-Ighil, R., Tounane, M., Iratni, A., *et al.* (2017) Optical, Structural and Photocatalysis Properties of Cu-Doped TiO_2 Thin Films. *Applied Surface Science*, **395**, 110-116. https://doi.org/10.1016/j.apsusc.2016.07.034

[33] Sato, S., Nakamura, R. and Abe, S. (2005) Visible-Light Sensitization of TiO_2 Photocatalysts by Wet-Method N Doping. *Applied Catalysis A: General*, **284**, 131-137. https://doi.org/10.1016/j.apcata.2005.01.028

[34] Qin, W., Lu, S., Wu, X. and Wang, S. (2013) Dye-Sensitized Solar Cell Based on N-Doped TiO_2 Electrodes Prepared on Titanium. *International Journal of Electrochemical Science*, **8**, 7984-7990. https://doi.org/10.1016/s1452-3981(23)12863-x

[35] Ansari, S.A., Khan, M.M., Ansari, M.O. and Cho, M.H. (2016) Nitrogen-Doped Titanium Dioxide (N-Doped TiO_2) for Visible Light Photocatalysis. *New Journal of Chemistry*, **40**, 3000-3009. https://doi.org/10.1039/c5nj03478g

[36] Tajizadegan, H., Heidary, A., Torabi, O., Golabgir, M.H. and Jamshidi, A. (2016) Synthesis and Characterization of $ZnCr_2O_4$ Nanospinel Prepared via Homogeneous Precipitation Using Urea Hydrolysis. *International Journal of Applied Ceramic Technology*, **13**, 289-294. https://doi.org/10.1111/ijac.12440

[37] Wang, Y., Bai, Y., Wu, C., Guo, J., Yu, X., Xu, K., *et al.* (2013) Nitrogen-Doped TiO_2 Nanocrystals for High-Performance Lithiumion Batteries. *Advanced Materials*, **25**, 1481-1486.

[38] Moyez, S.A. and Roy, S. (2018) Thermal Engineering of Lead-Free Nanostructured $CH_3NH_3SnCl_3$ Perovskite Material for Thin-Film Solar Cell. *Journal of Nanoparticle Research*, **20**, Article No. 5. https://doi.org/10.1007/s11051-017-4108-z

[39] Mansour, A.M., Nasr, M., Saleh, H.A. and Mahmoud, G.M. (2019) Physical Characterization of 5',5"-Dibromo-O-Cresolsulfophthalein (BCP) Spin-Coated Thin Films and BCP/P-Si Based Diode. *Applied Physics A*, **125**, Article No. 625. https://doi.org/10.1007/s00339-019-2920-2

[40] Husain, S., Keelani, A.O. and Khan, W. (2018) Influence of Mn Substitution on Morphological, Thermal and Optical Properties of Nanocrystalline $GdFeO_3$ Orthoferrite. *Nano-Structures & Nano-Objects*, **15**, 17-27. https://doi.org/10.1016/j.nanoso.2018.03.002

[41] Rejaiba, O., Khirouni, K., Dhaou, M.H., Alzahrani, B., Bouazizi, M.L. and Khelifi, J. (2022) Investigation Study of Optical and Dielectric Parameters Using Absorption and Diffuse Reflectance Spectroscopy Method on $La_{0.57}Nd_{0.1}Sr_{0.13}Ag_{0.2}MnO_3$ Perovskite for Optoelectronic Application. *Optical and Quantum Electronics*, **54**, Article No. 315.

[42] Kharrat, A.B.J., Kahouli, K. and Chaabouni, S. (2020) Detailed Investigation of the Optical Properties of the $(C_8H_{11}BrN)_3BiCl_6$ Compound by UV-Visible Measurements. *Bulletin of Materials Science*, **43**, Article No. 275. https://doi.org/10.1007/s12034-020-02248-7

[43] El Nahrawy, A.M., Hemdan, B.A., Mansour, A.M., Elzwawy, A. and AbouHammad, A.B. (2022) Structural and Opto-Magnetic Properties of Nickel Magnesium Copper Zircon Silicate Nano-Composite for Suppress the Spread of Foodborne Pathogenic Bacteria. *Silicon*, **14**, 6645-6660. https://doi.org/10.1007/s12633-021-01295-x

[44] Hemdan, B.A., El Nahrawy, A.M., Mansour, A.M. and Hammad, A.B.A. (2019) Green Sol-Gel Synthesis of Novel Nanoporous Copper Aluminosilicate for the Eradication of Pathogenic Microbes in Drinking Water and Wastewater Treatment. *Environmental Science and Pollution Research*, **26**, 9508-9523. https://doi.org/10.1007/s11356-019-04431-8

[45] Hcini, F., Hcini, S., Almoneef, M.M., Dhaou, M.H., Alshammari, M.S., Mallah, A., Zemni, S., Lefi, N. and Bouazizi, M.L. (2021) Thermal, Microstructural, Optical, Magnetic and Magnetocaloric Studies for $Ni_{0.5}Mn_{0.5}Cr_2O_4$ Chromite Spinel Prepared Using Sol-Gel Method. *Journal of Molecular Structure*, **1243**, Article 130769. https://doi.org/10.1016/j.molstruc.2021.130769

[46] Hcini, F., Hcini, S., Wederni, M.A., Alzahrani, B., Al Robei, H., Khirouni, K., Zemni, S. and Bouazizi, M.L. (2022) Structural, Optical, and Dielectric Properties for $Mg_{0.6}Cu_{0.2}Ni_{0.2}Cr_2O_4$ Chromite Spinel. *Physica B*: *Condensed Matter*, **624**, Article 413439. https://doi.org/10.1016/j.physb.2021.413439

[47] Mott, N.F. and Davis, E.A. (2012) Electronic Processes in Non-Crystalline Materials. Oxford University Press.

[48] Chen, Y., Zhang, Y., Wang, C., Ma, J., Li, X. and Yang, S. (2017) Improving the Electrochemical Performance of TiO_2 Anodes for Lithium-Ion Batteries by Nitrogen and Carbon Co-Doping. *Journal of Materials Chemistry A*, **5**, 1243-1250.